Formation of NiCo2V2O8 yolk – double shell spheres with enhanced lithium storage properties

Lu, Yan; Nai, Jianwei; Lou, David Xiong Wen

2018

Lu, Y., Nai, J., & Lou, D. X. W. (2018). Formation of NiCo2V2O8 yolk – double shell spheres with enhanced lithium storage properties. Angewandte Chemie International Edition, 57(11), 2899-2903. doi:10.1002/anie.201800363

https://hdl.handle.net/10356/137731

https://doi.org/10.1002/anie.201800363

Formation of $NiCo_2V_2O_8$ Yolk-Double-Shelled Spheres with Enhanced Lithium Storage Properties

*Yan Lu, Jianwei Nai, and Xiong Wen (David) Lou**

[*] Dr. Y. Lu, Dr. J. W. Nai, Prof. X. W. Lou

School of Chemical and Biomedical Engineering, Nanyang Technological University, 62 Nanyang Drive, Singapore 637459, Singapore

Email: xwlou@ntu.edu.sg; davidlou88@gmail.com

Webpage: http://www.ntu.edu.sg/home/xwlou/

Abstract

Complex nanostructures with multi-components and intricate architectures hold great potential in developing high-performance electrode materials for lithium-ion batteries (LIBs). Herein, we demonstrate a facile self-templating strategy for the synthesis of metal vanadate nanomaterials with complex chemical composition of $NiCo_2V_2O_8$ and a unique yolk-double-shelled structure. Starting with the Ni-Co glycerate spheres, $NiCo_2V_2O_8$ yolk-double-shelled spheres are synthesized through an anion-exchange reaction of Ni-Co glycerate templates with VO_3^- ions, followed by an annealing treatment. By virtue of compositional and structural advantages, these $NiCo_2V_2O_8$ yolk-double-shelled spheres manifest outstanding lithium storage properties when evaluated as anodes for LIBs. Impressively, an extra-high reversible capacity of 1228 mAh g^{-1} can be retained after 500 cycles at a high current density of 1.0 A g^{-1}.

Keywords: vanadates, hollow, yolk-shell, nanostructures, lithium-ion batteries

Lithium-ion batteries (LIBs) are currently the predominant power source for portable electronic devices and promising for electric vehicles in the near future because of their advantages of high energy density, long lifespan, as well as environmental benignity.[1-3] With substantial merits of high capacity, widespread availability and enhanced safety, metal oxides show great potential as electrode materials for next-generation high-performance LIBs.[4,5] Recently, ternary cobalt vanadates have shown remarkable electrochemical properties and emerged as a new class of oxide-based anodes for LIBs.[6-9] The strongly coupled conversion-type cobalt oxide and intercalation-type vanadium oxide endow the ternary cobalt vanadates with a conversion-intercalation-based lithium storage mechanism.[6] This unique hybrid mechanism offers cobalt vanadates higher capacities and lower volume changes over many other simple metal oxides during the lithiation/delithiation processes.[6,7,9] However, practical applications of cobalt vanadates are still hindered by the poor rate performance and capacity fading due to the low intrinsic electric conductivity, gradually reduced crystallinity, and inevitable volume changes during the prolonged cycling.[6,10,11]

To address these electrode-involved problems, a promising strategy is to rationally increase the compositional complexity of active materials.[5,12] Specifically, the introduction of alien metal cations into the crystal structure of a metal oxide/sulfide may bring more redox active sites and a certain degree of conductivity enhancement, thus effectively improve the reversible lithium storage performance.[5] For example, nickel has been conceived as a cost-effective and scalable alternative to partially replace the cobalt species in cobalt oxides/sulfides to improve the electrochemical performance.[12-14] Similarly, doping nickel ions into the lattice of cobalt vanadate is expected to be a possible way to promote the lithium storage properties. Nevertheless, it is highly challenging to fabricate complex quaternary Ni-Co vanadates. On the other hand, high electrochemical performance

can also be achieved by a delicate design and synthesis of electrode materials with proper architectures.[15-17] Particularly, hollow structures with intricate interiors, such as yolk-shelled and multi-shelled structures, have recently drawn tremendous attention in a wide range of applications.[15,18,19] In energy-related applications, it has been demonstrated that these complex hollow particles not only inherit the advantages of hollow nanostructures (e.g., high surface area, enhanced volume change accommodation and large electrode/electrolyte interface), but also improve weight fraction of active species, thus dramatically enhancing the energy density of the electrode materials.[20,21] Motivated by these merits, researchers have fabricated a variety of electrode materials on the basis of yolk-shelled or multi-shelled hollow structures, such as Ni-Co oxide yolk-shelled nanoprisms,[12] SnO_2 yolk-double-shelled spheres,[22] MoO_2/carbon triple-shelled spheres,[20] Co_3O_4 multi-shelled spheres,[23] $Co_3O_4@Co_3V_2O_8$ multi-shelled nanoboxes,[9] and Ni-Co oxide seven-layered particles.[24] However, most of the complex hollow particles reported so far possess relatively simple compositions. It is highly desirable, yet quite challenging, to develop effective strategies to prepare complex hollow structures with intricate compositions.

Herein, we develop a facile self-templating approach to synthesize novel quaternary $NiCo_2V_2O_8$ yolk-double-shelled spheres (YDSSs). A stepwise hollowing process assisted by anion-exchange is observed for the formation of the yolk-double-shelled structures. Moreover, effects of the composition of templates and the amount of vanadium source on the final hollow structures are investigated. Finally, we demonstrate that the $NiCo_2V_2O_8$ YDSSs show superior lithium storage properties as electrode materials for LIBs with high capacity and long cyclability.

The overall scheme of our strategy has two stages, as illustrated in **Figure 1**. Briefly, the Ni-Co glycerate template spheres with a size of ~500 nm (Figure S1-S2, Supporting Information)[25] are first

transformed into amorphous Ni-Co-V precursor YDSSs (Figure S2, Supporting Information) through an anion-exchange reaction between the Ni-Co glycerate precursor spheres and VO_3^- ions (Stage I). In stage II, these amorphous Ni-Co-V precursor YDSSs are further converted into crystalline $NiCo_2V_2O_8$ YDSSs through a subsequent thermal treatment. X-ray powder diffraction (XRD) analysis indicates the amorphous nature of the Ni-Co-V precursor YDSSs (Figure S3, Supporting Information). Field-emission scanning electron microscope (FESEM) image reveals that these Ni-Co-V precursor spheres inherit the morphology and size of their spherical templates but with a rougher surface (Figure S2d). As elucidated by transmission electron microscope (TEM) observation (Figure S2e, f), the Ni-Co-V precursor particles possess a solid core and two shells. A large cavity between the core and inner shell is observed, while a relatively narrow gap exists between the two shells.

An annealing treatment is then carried out to convert the amorphous Ni-Co-V precursor to crystalline $NiCo_2V_2O_8$ YDSSs. **Figure 2**a shows an overview FESEM image of the as-prepared $NiCo_2V_2O_8$ YDSSs. It is obvious that the sample retains the spherical morphology after the thermal treatment. A magnified FESEM image reveals that the surface of these spheres is composed of closely packed nanoparticles (Figure 2b), suggesting the occurrence of crystallization during the annealing process. The interior architecture of the $NiCo_2V_2O_8$ YDSSs is further elucidated by TEM as shown in Figure 2c,d. The yolk-double-shelled structures are well-retained after the annealing. The average diameter of the cores and the thickness of the inner and outer shells are about 90 nm, 90 nm, and 35 nm, respectively. A closer examination of a $NiCo_2V_2O_8$ YDSS reveals that the core and shells are composed of numerous small nanoparticles (Figure 2e). Benefitting also from the complex hollow nanostructure, the $NiCo_2V_2O_8$ YDSSs exhibit a large Brunauer-Emmett-Teller specific surface area

of 72.4 m^2 g^{-1} (Figure S4, Supporting Information). XRD pattern (Figure 2f) of the $NiCo_2V_2O_8$ YDSSs is similar to that of orthorhombic $Co_3V_2O_8$ phase (JCPDS card no. 74-1486) or orthorhombic $Ni_3V_2O_8$ phase (JCPDS card no. 70-1394). To further verify the crystal structure of the product, a better crystalline sample is obtained by treating the amorphous Ni-Co-V precursor sample at a higher temperature of 600 °C for 2 h. As shown in the XRD pattern (Figure S5, Supporting Information), the diffraction peaks are located between the corresponding peaks of the standard orthorhombic $Co_3V_2O_8$ and $Ni_3V_2O_8$, confirming the formation of a single phase of Ni-Co vanadate, i.e., orthorhombic $Ni_xCo_{3-x}V_2O_8$ phase. The lattice fringes with a *d*-spacing of 2.350 Å are measured in the outer shell of a $NiCo_2V_2O_8$ YDSS (Figure S6a, Supporting Information), which lies in between the *d*-spacing of 2.363 Å for (240) planes of $Co_3V_2O_8$ and *d*-spacing of 2.346 Å for (042) planes of $Ni_3V_2O_8$, suggesting the formation of a pure-phase Ni-Co vanadate. As revealed from the EDX analysis (Figure S7, Supporting Information), the Ni/Co molar ratio is about 1:2, which suggests the specific chemical composition of the product is $NiCo_2V_2O_8$. The elemental mapping results and line scans show the even distribution of Co and Ni elements throughout the whole particle, further confirming the single-phase character of the final products (Figure S8, Supporting Information).

Apparently, the annealing process (Stage II in Figure 1) will not alter the hollow nanostructures once the amorphous Ni-Co-V precursor YDSSs are formed. To reveal the hollowing mechanism during the anion-exchange process (Stage I in Figure 1) for the unique yolk-double-shelled structures, the process is monitored by time-dependent observations. XRD results of the intermediate samples collected at 10 min and 30 min (Figure S9, Supporting Information) reveal that the Ni-Co glycerate particles are transformed to amorphous status within 10 min of the reaction. In contrast, the structural evolution from the solid sphere to hollow sphere is much slower. During the reaction, the spheres

remain as smooth and solid particles when the reaction time reaches 10 min (Figure S10a,b, Supporting Information). As the time prolongs to 30 min, an obvious cavity appears inside each particle (Figure S10c,d, Supporting Information), leading to formation of a yolk-shelled structure with a small core encapsulated in a thick shell. By further increasing the reaction time to 1 h, the thick shell can split into two discrete layers with a narrow but well-defined gap between them (Figure S2e,f, Supporting Information). Meanwhile, the shrinkage of the core leads to further increase of the interior space between the core and the in-situ formed inner shell. Therefore, the overall structural evolution can be regarded as a stepwise hollowing process: the formation of the yolk-single-shelled structure and subsequent splitting of the shell structure from one into two layers. The inhomogeneous composition within the precursor solid spheres (Figure S2b,c, Supporting Information) might be responsible for the formation of the YDSSs,[26] which is then realized by the anion-exchange process.

We have also investigated the effect of the concentration of vanadium source on the structural evolution. As elucidated by the FESEM and TEM observations (Figure S11, Supporting Information), the presence of NH_4VO_3 plays a key role on the formation of hollow nanostructures. For example, urchin-like solid spheres are produced without the addition of vanadium source in the reaction system (Figure S11a,d, Supporting Information), suggesting that the anion-exchange induced outward mass diffusion should account for the formation of the hollow structures. When concentrations of 10 mM and 40 mM of NH_4VO_3 are used, yolk-shelled and single-shelled hollow structures are produced, respectively (Figure S11b,c,e,f, Supporting Information). In addition, the composition of the template also shows a crucial impact on the interior structure of the product. Specifically, pure cobalt glycerate spheres have also been adopted as the template for comparison (Figure S12, Supporting Information). Instead of the yolk-double-shelled structures, the as-derived Co-V precursor product is composed of

single-shelled hollow structures with a grainy surface (**Figure 3**a-c). Hence, the absence of the Ni^{2+} ions within the cobalt glycerate templates might change the composition distribution across the solid spheres, leading to different structural evolution processes during the ion-exchange reactions.[25,27] After a simple thermal treatment of the Co-V precursor hollow spheres (HSs) at 400 °C for 2 h, $Co_3V_2O_8$ HSs are successfully prepared (Figure 3d-f and Figure S13, Supporting Information). The measured *d*-spacing of 2.018 Å corresponds to (142) planes of $Co_3V_2O_8$ (Figure S6b, Supporting Information), further confirming the formation of $Co_3V_2O_8$.

The electrochemical performance of $NiCo_2V_2O_8$ YDSSs has been examined as the anode material for LIBs. Cyclic voltammetry (CV) measurement is first carried out to get an insight into the lithium storage mechanism of the $NiCo_2V_2O_8$ sample (Figure S14, Supporting Information). Notably, the CV curves of the $NiCo_2V_2O_8$ YDSSs are similar to those observed in the previous reported nanostructured vanadate electrodes.[6,28-30] Specifically, two pronounced cathodic peaks are observed in the first cycle, which are corresponding to the complex transformations of $NiCo_2V_2O_8$ to Co^0, Ni^0, and $Li_xV_2O_5$ upon the lithiation reaction, as well as the formation of solid electrolyte interface (SEI).[6,31-33] In the following measurements, the CV profiles overlap well, indicating the excellent stability of these hollow structures for reversible lithium storage.[6] The CV curves of $Co_3V_2O_8$ HSs (Figure S15, Supporting Information) exhibit similar profiles with that of $NiCo_2V_2O_8$ YDSSs, indicating they have a similar lithium storage mechanism. The small differences observed in the curves might be ascribed to the different chemical compositions for these two samples.

Figure 4a shows the representative galvanostatic discharge/charge profiles of $NiCo_2V_2O_8$ sample for the first two cycles at the current density of 0.2 A g^{-1} within a cut-off voltage window of 0.01-3.0 V. Two pronounced plateaus around 0.8 V and 0.4 V are found in the first discharge curve, which are

in good agreement with the CV curves (Figure S14, Supporting Information). Whereas, those voltage plateaus are nearly disappeared in the second cycle. The signal washout might be ascribed to the pulverization of the electrode materials from nanoparticles into numerous ultrafine nanoparticles during the lithiation process.[34] Notably, $NiCo_2V_2O_8$ YDSSs and $Co_3V_2O_8$ HSs have a set of similar charge-discharge voltage plateaus (Figure S16, Supporting Information), further confirming their similar lithium storage mechanism. In addition, the galvanostatic discharge/charge profiles of $NiCo_2V_2O_8$ YDSSs show no obvious changes even at a high current density of 1.0 A g^{-1} (Figure S16, Supporting Information), indicating excellent high-rate reaction kinetics of the materials.[35] The $NiCo_2V_2O_8$ YDSSs deliver an initial discharge capacity of 1926 mAh g^{-1} and charge capacity of 1146 mAh g^{-1}, corresponding to a Coulombic efficiency (CE) of 60%. The initial capacity loss might be attributed to the irreversible processes such as the formation of SEI layer and the decomposition of electrolyte,[36-38] which are common for most transition metal oxide anode materials.[12,39,40] It is noteworthy that the initial CE of $NiCo_2V_2O_8$ YDSSs is lower than that of $Co_3V_2O_8$ HSs (60% *vs.* 66%) (Figure S16, Supporting Information), which might be ascribed to the enhanced surface adsorption and irreversible trapping of inserted Li^+ ions by the former due to its larger specific surface area (Figure S4 and S17, Supporting Information).[41] In the second cycle, a high reversible discharge capacity of 1182 mAh g^{-1} is achieved, rendering a much higher CE of about 93%.

Next, we evaluate the rate performance of $NiCo_2V_2O_8$ YDSSs anode at various current densities (Figure 4b). Impressively, ultrahigh reversible capacities of 1354, 1146, 1005, 774, 613, and 388 mAh g^{-1} are achieved at current densities of 0.1, 0.5, 1, 2, 5 and 10 A g^{-1}, respectively. Moreover, when reducing the current density back to 0.1 A g^{-1}, the capacity quickly increases to 1127 mAh g^{-1}, indicating a good reversibility. Apparently, the $NiCo_2V_2O_8$ YDSSs demonstrate much improved rate

capability in terms of higher capacity at each current density compared to the $Co_3V_2O_8$ HSs, implying great advantages of the former sample in composition and structure.

The long-term cycling performance of $NiCo_2V_2O_8$ YDSSs at different current densities is also examined (Figure 4c,d). Particularly, the electrode is capable of delivering an ultrahigh reversible capacity of 1360 mAh g^{-1} after 80 cycles at a low current density of 0.2 A g^{-1}, exhibiting a high CE of around 98% throughout the cycling (Figure 4c). Interestingly, an increase in capacity is observed during the cycles. This phenomenon might be attributed to the improvement of Li^+ ion accessibility in the electrode materials during the cycling process, which would lead to an enhanced accommodation behaviour for lithium.[42,43] The overall structure of $NiCo_2V_2O_8$ YDSSs can be reasonably maintained after the cycling test (Figure S18, Supporting Information). In contrast, the $Co_3V_2O_8$ HSs exhibit a reversible capacity of only 623 mAh g^{-1} after 80 cycles at 0.2 A g^{-1}. In addition, when subjected to a higher current density of 1.0 A g^{-1}, the $NiCo_2V_2O_8$ YDSSs can still afford a high capacity of 1228 mAh g^{-1} after 500 cycles with remarkable stability (~100% CE) (Figure 4d).

Electrochemical impedance spectroscopy (EIS) measurements indicate that $NiCo_2V_2O_8$ YDSSs possess much lower charge transfer resistance and solid-state diffusion resistance than $Co_3V_2O_8$ HSs, as evidenced by the drastically reduced diameter of the semicircle at the high-medium frequency region and the obviously increased slope of the line in the low frequency region (Figure S19, Supporting Information). As a result, electron transfer and Li^+ ion diffusion are greatly facilitated to give the enhanced electrochemical performance of $NiCo_2V_2O_8$ YDSSs. Furthermore, $NiCo_2V_2O_8$ YDSSs also show much superior lithium storage properties than $NiCo_2O_4$ core-in-double-shell hollow spheres (CIDS HSs) prepared from the direct annealing of Ni-Co glycerate spheres in air,[44] demonstrating the great compositional advantages of $NiCo_2V_2O_8$ YDSSs toward lithium storage.

Overall, the $NiCo_2V_2O_8$ YDSSs exhibit outstanding lithium storage properties compared with the $Co_3V_2O_8$ HSs, $NiCo_2O_4$ CIDS HSs,[44] and many previously reported metal vanadate-based nanostructures (Table S1, Supporting Information), which could be attributed to the following reasons. First, the nano-sized structural subunits effectively facilitate the electronic/Li^+ ion transport in the electrode materials, ensuring better electrochemical activities. Second, the multi-level cavities between different shells can not only increase the electrode/electrolyte contact area but also accommodate the strain from the lithium insertion/extraction, contributing to the high rate capability and long cycle life. Furthermore, the increased compositional complexity in $NiCo_2V_2O_8$ YDSSs may further enhance the conductivity and enrich the redox centers.

In summary, we have demonstrated a facile strategy for the fabrication of a complex metal vanadate particles with quaternary $NiCo_2V_2O_8$ composition and yolk-double-shelled nanostructures. The synthesis involves the anion-exchange reaction between Ni-Co glycerate and VO_3^- ions under reflux condition, followed by a thermal treatment in air. Benefiting from the unique compositional and structural advantages, the as-prepared $NiCo_2V_2O_8$ YDSSs exhibit excellent electrochemical properties as anode materials for lithium-ion batteries with very high capacities, superior rate capability and excellent cycling stability. The present work might shed some light on the feasible synthesis of complex nanostructures for more complex compositions for different applications.

Acknowledgements

X. W. L. acknowledges the funding support from the National Research Foundation (NRF) of Singapore via the NRF Investigatorship (NRF-NRFI2016-04).

References

[1] D. Larcher, J. M. Tarascon, *Nat Chem* **2015**, *7*, 19.

[2] B. Dunn, H. Kamath, J. M. Tarascon, *Science* **2011**, *334*, 928.

[3] M. A. Hannan, M. M. Hoque, A. Mohamed, A. Ayob, *Renew Sust Energ Rev* **2017**, *69*, 771.

[4] G. Chen, L. T. Yan, H. M. Luo, S. J. Guo, *Adv. Mater.* **2016**, *28*, 7580.

[5] Y. Zhao, X. F. Li, B. Yan, D. B. Xiong, D. J. Li, S. Lawes, X. L. Sun, *Adv. Energy Mater.* **2016**, *6*, 1502175.

[6] G. Z. Yang, H. Cui, G. W. Yang, C. X. Wang, *ACS Nano* **2014**, *8*, 4474.

[7] F. F. Wu, C. H. Yu, W. X. Liu, T. Wang, J. K. Feng, S. L. Xiong, *J. Mater. Chem. A* **2015**, *3*, 16728.

[8] C. Zhu, Z. Q. Liu, J. Wang, J. Pu, W. L. Wu, Q. W. Zhou, H. G. Zhang, *Small* **2017**, *13*, 1701260.

[9] Y. Lu, L. Yu, M. Wu, Y. Wang, X. W. Lou, *Adv. Mater.* **2018**, *30*, 1702875.

[10] X. L. Liu, Y. C. Cao, H. Zheng, X. Chen, C. Q. Feng, *Appl. Surf. Sci.* **2017**, *394*, 183.

[11] C. Lv, J. X. Sun, G. Chen, C. S. Yan, D. H. Chen, *Nano Energy* **2017**, *33*, 138.

[12] L. Yu, B. Y. Guan, W. Xiao, X. W. Lou, *Adv. Energy Mater.* **2015**, *5*, 1500981.

[13] J. F. Li, S. L. Xiong, Y. Y. Liu, Z. C. Ju, Y. T. Qian, *ACS Appl. Mater. Interfaces* **2013**, *5*, 981.

[14] L. F. Shen, Q. Che, H. S. Li, X. G. Zhang, *Adv. Funct. Mater.* **2014**, *24*, 2630.

[15] L. Yu, H. Hu, H. B. Wu, X. W. Lou, *Adv. Mater.* **2017**, *29*, 1604563.

[16] L. Cong, H. Xie, J. Li, *Adv. Energy Mater.* **2017**, *7*, 1601906.

[17] Y. Xu, M. Zhou, Y. Lei, *Adv. Energy Mater.* **2016**, *6*, 1502514.

[18] X. Wang, J. Feng, Y. Bai, Q. Zhang, Y. Yin, *Chem. Rev.* **2016**, *116*, 10983.

[19] X. W. Lou, L. A. Archer, Z. Yang, *Adv. Mater.* **2008**, *20*, 3987.

[20] Y. W. Wang, L. Yu, X. W. Lou, *Angew. Chem. Int. Ed.* **2016**, *55*, 14668.

[21] S. Xu, C. M. Hessel, H. Ren, R. Yu, Q. Jin, M. Yang, H. Zhao, D. Wang, *Energy Environ. Sci.* **2014**, *7*, 632.

[22] Y. J. Hong, M. Y. Son, Y. C. Kang, *Adv. Mater.* **2013**, *25*, 2279.

[23] X. Wang, X. L. Wu, Y. G. Guo, Y. T. Zhong, X. Q. Cao, Y. Ma, J. N. Yao, *Adv. Funct. Mater.* **2010**, *20*, 1680.

[24] B. Y. Guan, A. Kushima, L. Yu, S. Li, J. Li, X. W. Lou, *Adv. Mater.* **2017**, *29*, 1605902.

[25] L. F. Shen, L. Yu, H. B. Wu, X. Y. Yu, X. G. Zhang, X. W. Lou, *Nat. Commun.* **2015**, *6*, 6694.

[26] D. S. Bin, Z. X. Chi, Y. T. Li, K. Zhang, X. Z. Yang, Y. G. Sun, J. Y. Piao, A. M. Cao, L. J. Wan, *J. Am. Chem. Soc.* **2017**, *139*, 13492.

[27] B. Liu, H. C. Zeng, *Small* **2005**, *1*, 566.

[28] Y. Z. Luo, X. Xu, X. C. Tian, Q. L. Wei, M. Y. Yan, K. N. Zhao, X. M. Xu, L. Q. Mai, *J. Mater. Chem. A* **2016**, *4*, 5075.

[29] V. Soundharrajan, B. Sambandam, J. Song, S. Kim, J. Jo, S. Kim, S. Lee, V. Mathew, J. Kim, *ACS Appl. Mater. Interfaces* **2016**, *8*, 8546.

[30] J. Xiang, X. Y. Yu, U. Paik, *J. Power Sources* **2016**, *329*, 190.

[31] P. Poizot, S. Laruelle, S. Grugeon, L. Dupont, J. M. Tarascon, *Nature* **2000**, *407*, 496.

[32] D. Bresser, S. Passerini, B. Scrosati, *Energy Environ. Sci.* **2016**, *9*, 3348.

[33] J. Liu, H. Xia, D. F. Xue, L. Lu, *J. Am. Chem. Soc.* **2009**, *131*, 12086.

[34] L. Xu, C. Kim, A. K. Shukla, A. Dong, T. M. Mattox, D. J. Milliron, J. Cabana, *Nano Lett.* **2013**, *13*, 1800.

[35] G. Zhou, E. Paek, G. S. Hwang, A. Manthiram, *Nat. Commun.* **2015**, *6*, 7760.

[36] J. Cabana, L. Monconduit, D. Larcher, M. R. Palacin, *Adv. Mater.* **2010**, *22*, E170.

[37] S. Laruelle, S. Grugeon, P. Poizot, M. Dolle, L. Dupont, J. M. Tarascon, *J. Electrochem. Soc.* **2002**, *149*, A627.

[38] R. Dedryvère, L. Gireaud, S. Grugeon, S. Laruelle, J. M. Tarascon, D. Gonbeau, *J. Phys. Chem. B* **2005**, *109*, 15868.

[39] Z. Y. Wang, D. Y. Luan, S. Madhavi, Y. Hu, X. W. Lou, *Energy Environ. Sci.* **2012**, *5*, 5252.

[40] B. Liu, J. Zhang, X. F. Wang, G. Chen, D. Chen, C. W. Zhou, G. Z. Shen, *Nano Lett.* **2012**, *12*, 3005.

[41] S. H. Ng, J. Wang, D. Wexler, K. Konstantinov, Z. P. Guo, H. K. Liu, *Angew. Chem. Int. Ed.* **2006**, *45*, 6896.

[42] L. Xia, S. Q. Wang, G. X. Liu, L. X. Ding, D. D. Li, H. H. Wang, S. Z. Qiao, *Small* **2016**, *12*, 853.

[43] X. Zhou, L. J. Wan, Y. G. Guo, *Adv. Mater.* **2013**, *25*, 2152.

[44] L. Shen, L. Yu, X. Y. Yu, X. Zhang, X. W. Lou, *Angew. Chem. Int. Ed.* **2015**, *54*, 1868.

Figures and Captions

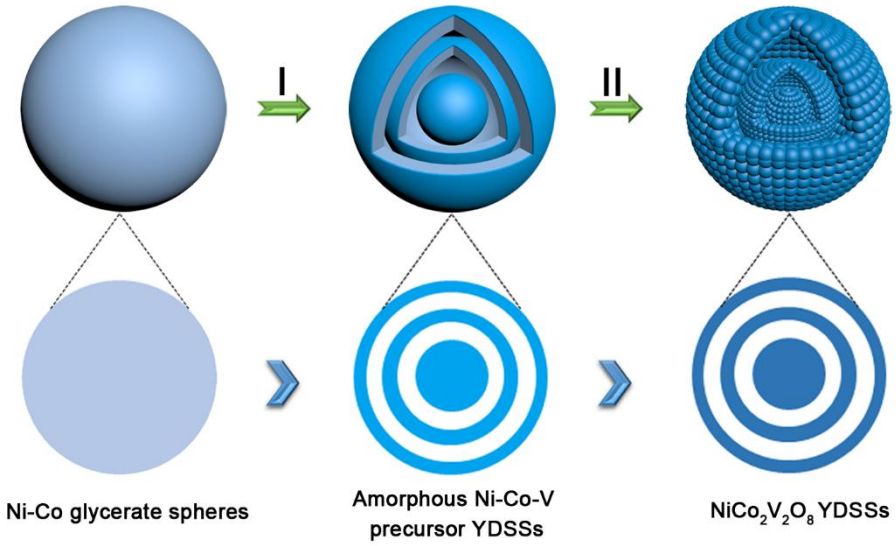

Figure 1. Schematic illustration for the synthesis of $NiCo_2V_2O_8$ YDSSs. Stage I: The formation of amorphous Ni-Co-V precursor YDSSs through an anion-exchange reaction; Stage II: Thermal treatment to generate $NiCo_2V_2O_8$ YDSSs.

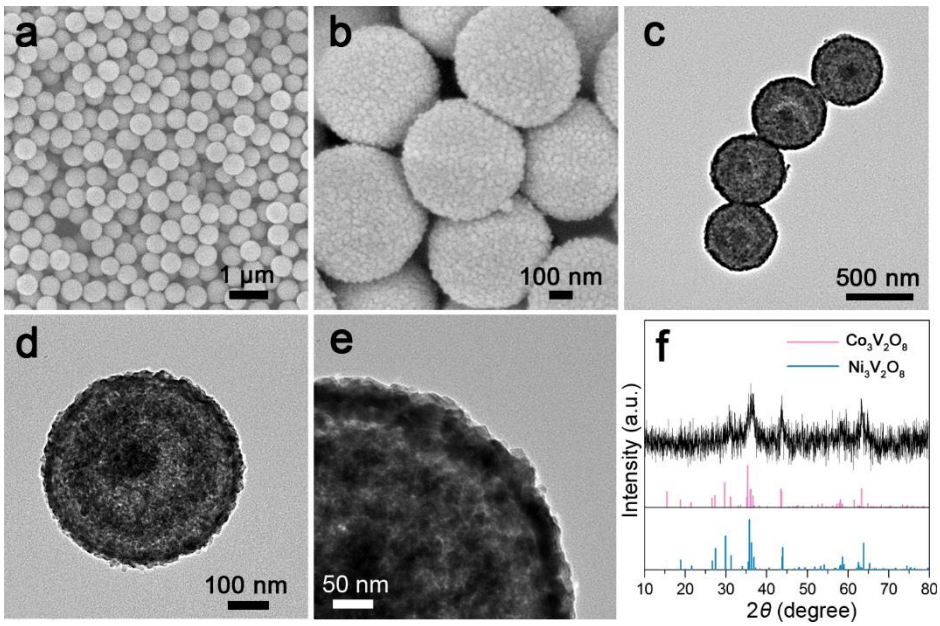

Figure 2. a,b) FESEM images, c-e) TEM images, and f) XRD pattern of the $NiCo_2V_2O_8$ YDSSs.

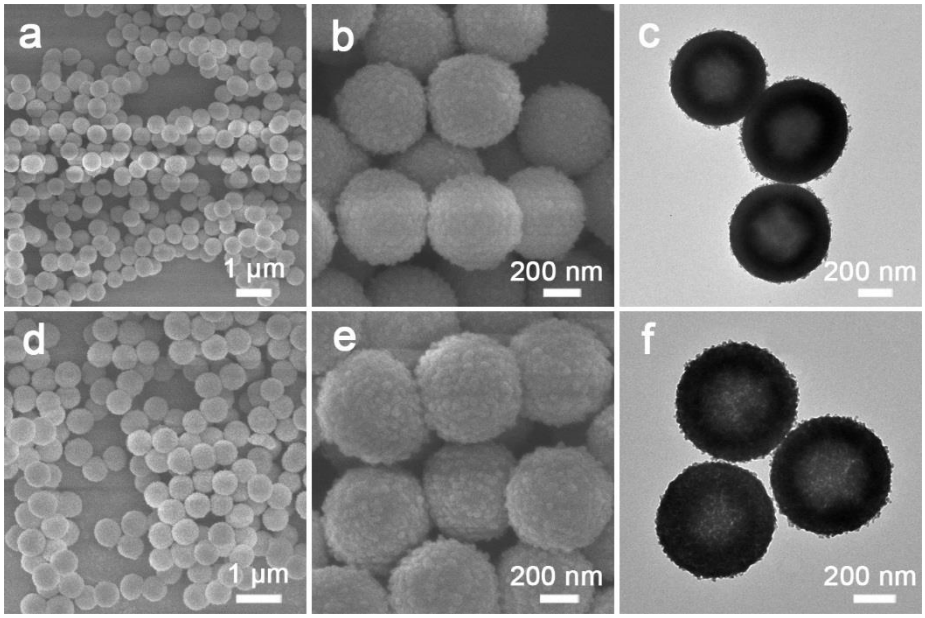

Figure 3. a,b,d,e) FESEM and c,f) TEM images of (a-c) Co-V precursor HSs, and (d-f) $Co_3V_2O_8$ HSs.

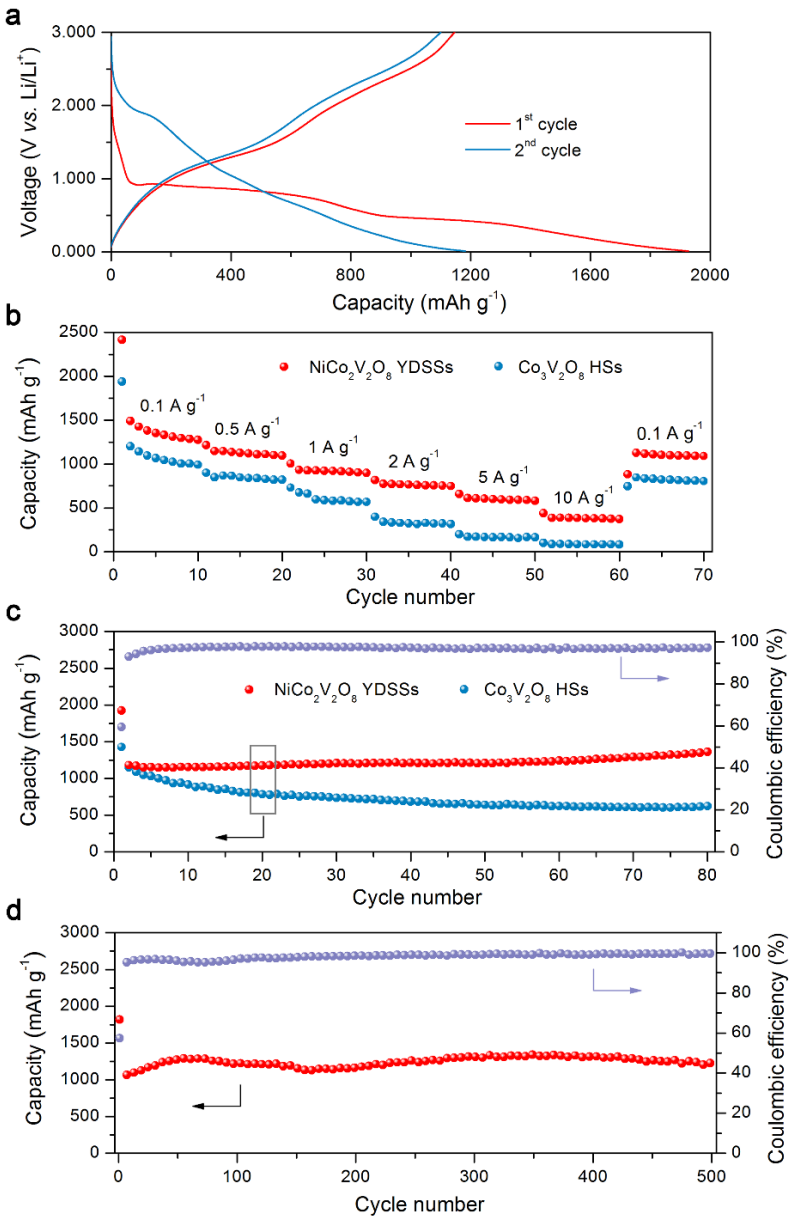

Figure 4. Electrochemical lithium storage properties of the $NiCo_2V_2O_8$ and $Co_3V_2O_8$ samples. a) Galvanostatic charge-discharge voltage profiles of the $NiCo_2V_2O_8$ electrode at 0.2 A g^{-1}. b) Rate capabilities of the $NiCo_2V_2O_8$ and $Co_3V_2O_8$ electrodes. c) Cycling performance of the $NiCo_2V_2O_8$ and $Co_3V_2O_8$ electrodes at 0.2 A g^{-1} and the corresponding Coulombic efficiency for the $NiCo_2V_2O_8$ electrode. d) High-rate cycling performance and the corresponding Coulombic efficiency of the $NiCo_2V_2O_8$ electrode at 1.0 A g^{-1}. All measurements were conducted in the voltage range of 0.01-3.0 V *vs.* Li/Li^+.

for Table of Content Entry

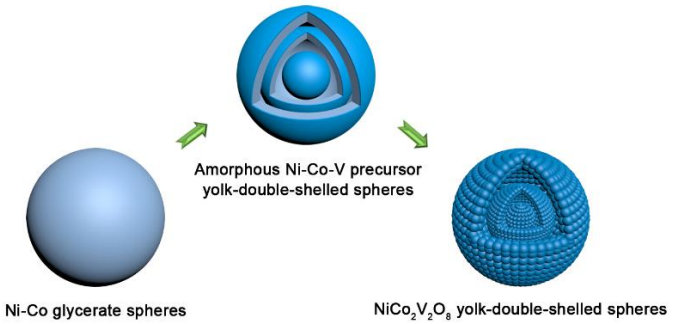

Yolk-double-shelled $NiCo_2V_2O_8$ spheres have been successfully synthesized via a facile self-templating approach utilizing the ion-exchange reaction between Ni-Co glycerate spheres and NH_4VO_3 under reflux conditions, followed by a thermal treatment in air. Benefiting from the desirable structural and compositional advantages, the as-synthesized $NiCo_2V_2O_8$ samples exhibit outstanding electrochemical properties when evaluated as an anode material for lithium-ion batteries.